Antireflection Coating Using Metamaterials and Identification of Its Mechanism

Hou-Tong Chen,* Jiangfeng Zhou, John F. O'Hara, Frank Chen, Abul K. Azad, and Antoinette J. Taylor

MPA-CINT, MS K771, Los Alamos National Laboratory, Los Alamos, New Mexico 87545, USA

(Received 30 January 2010; revised manuscript received 24 June 2010; published 9 August 2010)

We present a novel approach of antireflection coating using metamaterials. It dramatically reduces the reflection and greatly enhances the transmission near a specifically designed frequency over a wide range of incidence angles for both transverse magnetic and transverse electric polarizations. A classical interference mechanism is identified through analytical derivations and numerical simulations. It elucidates that the tailored magnitude and phase of waves reflected and transmitted at boundaries of metamaterial coating are responsible for the antireflection.

DOI: 10.1103/PhysRevLett.105.073901 PACS numbers: 42.79.Wc, 42.25.Hz, 78.67.Pt, 78.20.Bh

When propagating electromagnetic waves encounter an interface of two media with different refractive indices, some portion of energy is reflected back and the rest transmits through. This well-known phenomenon is the basis of numerous optical technologies and is described by Snell's law and Fresnel equations. In many applications however, reflection is undesirable and causes, for example, insertion losses or Fabry-Pérot fringes. Antireflection coatings using single or multiple layered dielectric films have long been the solution in the optical regime. Single layered quarter-wave antireflection coatings require a particular refractive index and a quarter wavelength thickness. This approach is scalable over a wide spectral range, but it is limited by natural material properties. For example, in the far infrared and microwave bands, substrate materials such as semiconductors and ceramics often have large refractive indices, which makes it difficult to find appropriate coating materials that satisfy the index matching requirement. Furthermore, it is often quite challenging to fabricate high quality and relatively thick films required for long wavelengths.

Antireflection coatings are of additional importance when considering the generally low power in many far infrared or terahertz (THz) systems. There have been a few efforts to develop antireflection coatings at THz frequencies, which include (i) quarter-wave antireflection, e.g., by optical lapping [1], polymer coatings [2], or using artificial dielectric metamaterials [3], (ii) artificial dielectric structures (surface relief structures) to achieve impedance matching with a gradient index [4] or by creating an effective index value satisfying quarter-wave antireflection [5], and (iii) thin metal films having very precisely controlled thickness [6,7]. All these approaches suffer from severe limitations; for instance, surface relief structures demand special fabrication procedures, in addition to the fact that substrate surfaces are no longer flat or smooth, limiting their application to many photonic devices.

Antireflection coatings operate by overcoming the mismatch between intrinsic impedances $Z_i = \sqrt{\mu_i/\epsilon_i}$ of two media, where ϵ_i and μ_i are the media electric permittivity and magnetic permeability, respectively. Metamaterials have inspired electromagnetic invisibility [8,9] due to the independently tailored ϵ and μ [10,11], which were assumed to also be responsible for enhanced light absorption [12,13]. In principle, by tuning the effective ϵ and μ, metamaterials should also be able to match media impedances and thereby alleviate the nonavailability of natural materials with the required index of refraction. But so far the general concept of metamaterials still suffers from high loss. Three-dimensional fabrication is another challenge. In this Letter, we present a novel approach of metamaterial antireflection coating, which does not suffer from high losses and thick coating, and involves only planar fabrication. We observed almost zero reflection and significantly enhanced transmission at a targeted frequency over a wide range of incidence angles for both transverse magnetic (TM) and transverse electric (TE) polarizations. We further identified that the underlying mechanism does not involve the magnetic response in metamaterials [12,13].

The experimental demonstration has been focused in the THz frequency range where antireflection coatings are still challenging. The metamaterial antireflection coatings consist of an array of gold electric split-ring resonators (SRRs) [14] and a gold mesh [15] patterned using conventional photolithography methods, and separated by a spacer layer of spin-coated and thermally cured polyimide (dielectric constant ~3.5) [13]. They were fabricated on intrinsic gallium arsenide (GaAs) substrates, with a unit cell schematically shown in Fig. 1(a), where the fourfold symmetry makes it polarization insensitive under normal incidence. In this design, the metal lines are 4 μm wide, 200 nm thick, and the SRRs have outer dimensions of 36 μm, 4 μm gaps, and 46 μm periodicity. The polyimide spacer thickness was expected to be about 13 μm. The metamaterial antireflection coatings were characterized at various incidence angles for both TM and TE polarizations, through reflection and transmission measurements using a fiber-coupled THz time-domain spectrometer [16].

Since our THz time-domain spectrometer cannot directly measure the reflection under normal incidence, it was determined by taking the advantage of echo pulses in the transmitted time-domain data. Echo pulses are gener-

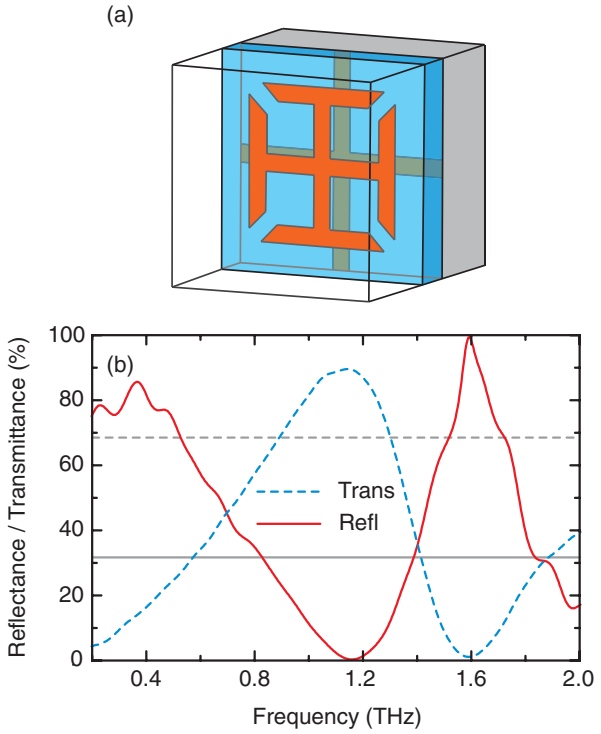

FIG. 1 (color online). (a) Schematic design of the metamaterial antireflection coating. (b) Experimentally measured reflectance and transmittance under normal incidence. The solid and dashed gray straight lines are the expected THz reflectance and transmittance, respectively, of a bare GaAs surface.

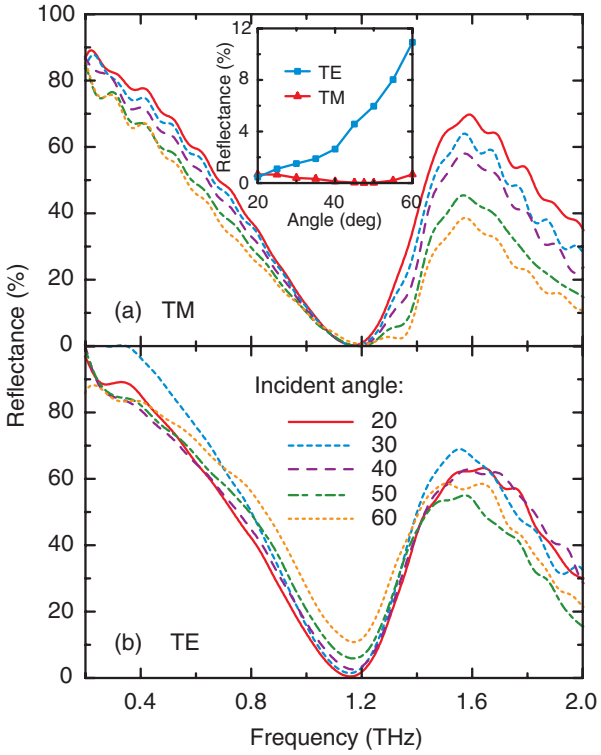

FIG. 2 (color online). Experimental results of reflectance spectra from the metamaterial-coated GaAs surface for (a) TM and (b) TE polarized incident THz radiation at various incidence angles. Inset: Angular dependent reflectance at the antireflection frequency.

ated by multiple reflections of the impulsive THz radiation between the two reflecting GaAs surfaces (with the front surface coated). As a result, the echoes measure the reflection of THz radiation that is incident on the coating from the GaAs side. However, simulations have shown it is almost identical to that incident from the air side. In Fig. 1(b) we observed a reflectance minimum of 0.32% near 1.2 THz, as compared to 32% reflectance from a bare GaAs surface. The transmittance under normal incidence was also measured, from which we obtained a transmittance maximum of 90% as compared to 68% through a bare air-GaAs interface. Without any optimization, the reflectance reduction and transmittance enhancement are already remarkable. The total loss of ~10% is also significantly smaller than in very thin metal film coatings [6,7] where the loss was ~60%.

Angular dependent reflectance spectra were directly measured and are shown in Fig. 2, with measured incidence angles ranging from 20° to 60°, limited by the mechanical layout of the THz spectrometer, and the sample (1 cm × 1 cm) and illumination (beam diameter ~3 mm) spot sizes. In Fig. 2(a) we show the reflectance spectra under TM polarization, where the frequency of the reflectance minimum has a negligible shift with the incident angles. The reflectance minimum decreases first with incidence angles, from 0.25% at 20° approaching nearly zero (0.005%) at 47.5°, and then it increases to 0.64% at 60°, as shown in the inset to Fig. 2(a) plotted at the fixed antireflection frequency. For a bare GaAs surface, the reflectance values are 27.2% at 20° and 8.7% at 60°. In Fig. 2(b) we show the reflectance spectra under TE polarization. The reflectance at the antireflection frequency is 0.46% at 20°, and it gradually and monotonically increases to 10.9% at 60°. Although the reflectance for TE polarization is larger than for TM polarization, particularly at increasing incidence angles, it significantly reduces the reflectance relative to a bare GaAs surface, which yields 34% at 20° and 56% at 60°. The reflectance values at small incidence angles are consistent with that under the normal incidence shown in Fig. 1(b), which indicates that the metamaterial antireflection coatings are effective for both light propagating directions, in contrast to only one direction antireflection with thin metal film coatings [6,7].

Finite-element numerical simulations were carried out using CST Microwave Studio 2009, to elucidate the roles of the SRRs, mesh, and spacer in achieving good antireflection performance. The unit cell shown in Fig. 1(a) was used with appropriate boundary conditions. The simulations resulted in complex S parameters, from which we obtained the frequency dependent reflectance $R = |S_{11}|^2$ and transmittance $T = |S_{21}|^2$. We first investigated the reflectance and transmittance under normal incidence as a function of the spacer thickness ranging from 4 μm to

16 μm. In these simulations, intrinsic GaAs was modeled as a lossless dielectric material with $\epsilon_{\text{GaAs}} = 12.7$, gold was simulated as a lossy metal with the default conductivity $\sigma = 4 \times 10^7$ S/m, and the spacer layer was treated as low loss dielectrics with $\epsilon_{\text{spacer}} = 1.5$ and $\tan\delta = 0.01$. It is worth noting that such a spacer material we purposely chose here, by itself, could never function as a good conventional antireflection coating.

From the simulation results shown in Fig. 3(a), we found there is an optimized spacer thickness approximately 9 μm ($\sim\lambda/18$) with which nearly zero reflectance and enhanced transmittance can be achieved. Deviation from this optimized spacer thickness results in a degraded antireflection performance and a shift in antireflection frequency. The simulations also revealed that nearly zero reflectance can always be achieved with lossy metal and spacer materials; losses mainly limit the transmittance enhancement. Although here the spacer dielectric constant of 1.5 was used, which alters the antireflection frequency as compared to the experiments, similar results were obtainable for any spacer dielectric constant, even ones larger than the substrate. Upon an additional increase of half wavelength in the spacer thickness, where the direct interaction between the SRRs and mesh is negligible, the metamaterial coating again exhibits antireflection behavior in Fig. 3, which suggests that the magnetic response [17,18] is not responsible for the metamaterial antireflection coatings. These findings inspire us to look for an alternative interpretation.

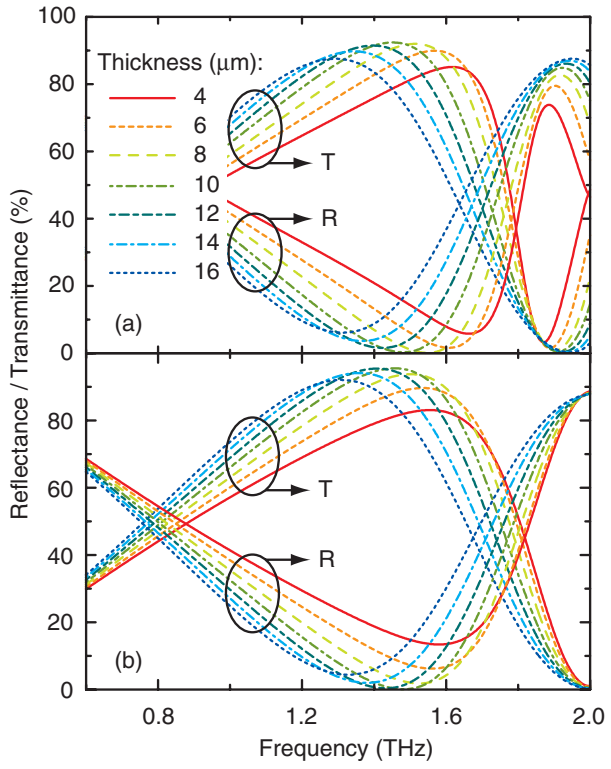

FIG. 3 (color online). (a) Numerically simulated and (b) theoretically calculated reflectance (solid curves) and transmittance (dashed curves) under normal incidence as a function of spacer thickness.

Additional simulations have reproduced the angular dependent reflectance in Fig. 2. The overall agreement with experimental results also validates the simulations and forms the basis for the theoretical model described below. The simulation results revealed that the different behaviors in the angular dependent reflectance between TM and TE polarizations are due to the spacer thickness; i.e., the polyimide spacer thickness in the fabricated metamaterial antireflection coating is a little smaller than the optimized value. With an optimized spacer thickness, the angular dependence exhibits almost identical behavior for both polarizations. If the spacer thickness increases to exceed the optimized value, the angular dependence will be reversed for TM and TE polarizations.

In order to further elucidate the antireflection mechanism, we modeled the SRR array and mesh as tuned-impedance interfaces with effectively zero thickness [19,20]. The modified air-spacer and spacer-substrate interfaces impart strong magnitude and phase shifts to the reflection and transmission coefficients. The whole antireflection system is depicted in Fig. 4(a), where the overall reflection and transmission are then superpositions of the multiple reflections and transmissions [21] at the two interfaces, i.e., the metamaterial coating boundaries:

$$\tilde{r} = \frac{r_{12}e^{i\phi_{12}} - r_{12}r_{21}r_{23}e^{i\zeta_1} + t_{12}r_{23}t_{21}e^{i\zeta_2}}{1 - r_{21}r_{23}e^{i(\phi_{21}+\phi_{23}+2\beta)}}, \quad (1)$$

$$\tilde{t} = \frac{t_{12}t_{23}e^{i(\theta_{12}+\theta_{23}+\beta)}}{1 - r_{21}r_{23}e^{i(\phi_{21}+\phi_{23}+2\beta)}}, \quad (2)$$

where variables illustrated in Fig. 4(a) indicate their meanings, $\zeta_1 = \phi_{12} + \phi_{21} + \phi_{23} + 2\beta$, $\zeta_2 = \theta_{12} + \phi_{23} + \theta_{21} + 2\beta$, $\beta = -\sqrt{\tilde{\epsilon}_{\text{spacer}}}k_0 d/\cos(\alpha_s)$, k_0 is the free space wave number, and $\alpha_s = \arcsin[\sin\alpha_i/\sqrt{\epsilon_{\text{spacer}}}]$ for arbitrary incidence angle α_i.

The reflection and transmission coefficients at individual interfaces can be derived from numerical simulations of the isolated SRR and mesh layers; i.e., mesh and GaAs substrate were removed from the unit cell [Fig. 1(a)] for the SRR interface, and SRR and air were removed for the mesh interface simulations. The reflectance and transmittance were then calculated by using Eqs. (1) and (2) with the simulated complex reflection and transmission coefficients. The calculation results are shown in Fig. 3(b), which superbly reproduce the spacer thickness dependent antireflection shown in Fig. 3(a). The model calculations suggest that the multiple reflections and transmissions in the metamaterial coating, rather than the magnetic response [17,18] (together with the electric response), are responsible for the reflection reduction and transmission enhancement. Further model calculations revealed that such a mechanism is also responsible for the perfect metamaterial absorbers [12,13] and electromagnetic-wave tunneling [22].

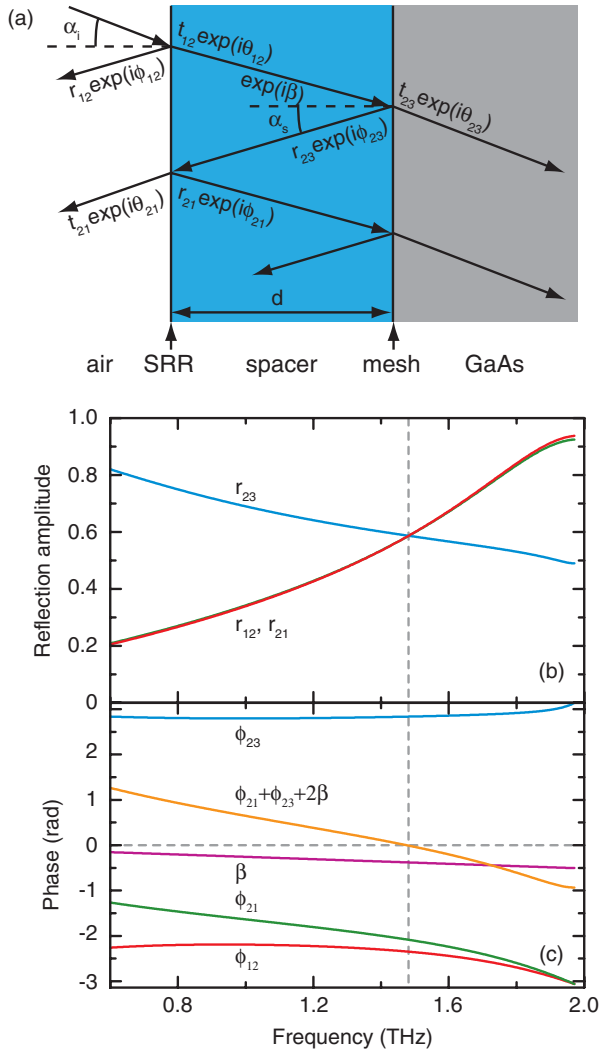

FIG. 4 (color online). (a) Illustration of interference model of the metamaterial antireflection coating and associated variables. (b) The magnitude and (c) phase of the complex reflection coefficients at the individual boundaries under normal incidence. The vertical dashed line indicates the optimized antireflection frequency.

From an application point of view, Eq. (1) may be still too complicated to guide the design of metamaterial antireflection coatings. If lossless materials are assumed, it can be simplified as

$$\tilde{r} = \frac{r_{21}\exp(i\phi_{12}) - r_{23}\exp[i(\phi_{12} + \phi_{21} + \phi_{23} + 2\beta)]}{1 - r_{21}r_{23}\exp[i(\phi_{21} + \phi_{23} + 2\beta)]}, \tag{3}$$

from which the antireflection conditions are (i) $r_{12} = r_{21} = r_{23}$ and (ii) $\phi_{21} + \phi_{23} + 2\beta = 2m\pi$, where m can be any integer. We plotted in Figs. 4(b) and 4(c) the magnitude and phase of the relevant reflection coefficients, with losses already considered, for normal incidence to verify the above antireflection conditions. We found that the increasing r_{21} and decreasing r_{23} cross each other, which satisfies the condition (i), and the phases exhibit similar values but with opposite signs, which can be compensated by a propagation phase 2β to simultaneously fulfill the condition (ii). These findings further suggest that many metamaterial structures including frequency selective surfaces could be used for antireflection coatings.

In conclusion, we have experimentally demonstrated metamaterial antireflection coatings achieving nearly zero reflection and significantly enhanced transmission over a wide range of incidence angles, for both TM and TE polarizations. Through analytical derivations and finite-element numerical simulations, we identified that the destructive and constructive interferences, respectively, due to the multiple reflections and transmissions in the metamaterial coatings, are responsible for the reduction of reflection and enhancement of transmission. This mechanism is also able to explain the perfect metamaterial absorbers and electromagnetic wave tunneling.

We acknowledge the Los Alamos National Lab LDRD Program and the Center for Integrated Nanotechnologies.

*chenht@lanl.gov

[1] K. Kawase, N. Hiromoto, and M. Fujiwara, Electron. Commun. Jpn. 2, Electron. **83**, 10 (2000).
[2] A. J. Gatesman *et al.*, IEEE Microwave Guided Wave Lett. **10**, 264 (2000).
[3] J. Zhang *et al.*, Appl. Opt. **48**, 6635 (2009).
[4] Y. W. Chen, P. Y. Han, and X.-C. Zhang, Appl. Phys. Lett. **94**, 041 106 (2009).
[5] A. Wagner-Gentner, U. U. Graf, D. Rabanus, and K. Jacobs, Infrared Phys. Technol. **48**, 249 (2006).
[6] J. Kröll, J. Darmo, and K. Unterrainer, Opt. Express **15**, 6552 (2007).
[7] A. Thoman, A. Kern, H. Helm, and M. Walther, Phys. Rev. B **77**, 195405 (2008).
[8] D. Schurig *et al.*, Science **314**, 977 (2006).
[9] J. Li and J. B. Pendry, Phys. Rev. Lett. **101**, 203901 (2008).
[10] D. R. Smith *et al.*, Phys. Rev. Lett. **84**, 4184 (2000).
[11] R. A. Shelby, D. R. Smith, and S. Schultz, Science **292**, 77 (2001).
[12] N. I. Landy *et al.*, Phys. Rev. Lett. **100**, 207402 (2008).
[13] H. Tao *et al.*, Opt. Express **16**, 7181 (2008).
[14] H.-T. Chen *et al.*, Opt. Express **15**, 1084 (2007).
[15] R. Ulrich, Infrared Phys. **7**, 37 (1967).
[16] J. F. O'Hara *et al.*, J. Nanoelectron. Optoelectron. **2**, 90 (2007).
[17] S. Zhang *et al.*, Phys. Rev. Lett. **95**, 137404 (2005).
[18] V. M. Shalaev *et al.*, Opt. Lett. **30**, 3356 (2005).
[19] C. L. Holloway *et al.*, Metamaterials **3**, 100 (2009).
[20] J. F. O'Hara *et al.*, Act. Passive Electron. Compon. **2007**, 1 (2007).
[21] M. Born and E. Wolf, *Principles of Optics* (Pergamon Press, New York, 1980), 6th ed.
[22] L. Zhou, W. Wen, C. T. Chan, and P. Sheng, Phys. Rev. Lett. **94**, 243905 (2005).